Computers in Biology and Medicine 202 (2026) 111435

Contents lists available at ScienceDirect

Computers in Biology and Medicine

journal homepage: www.elsevier.com/locate/compbiomed

Personalized computational hemodynamic analysis in transcatheter aortic valve: investigation of long-term degeneration

Luca Crugnola [a,*], Chiara Catalano [b], Laura Fusini [c,d], Salvatore Pasta [e,b], Gianluca Pontone [c,f], Christian Vergara [a]

[a] LaBS, Dipartimento di Chimica, Materiali e Ingegneria Chimica "Giulio Natta", Politecnico di Milano, Piazza Leonardo da Vinci 32, Milan, 20133, Italy
[b] Department of Research, IRCCS ISMETT, Via Tricomi, 5, Palermo, 90127, Italy
[c] Department of Perioperative Cardiology and Cardiovascular Imaging, Centro Cardiologico Monzino IRCCS, Via Carlo Parea 4, Milan, 20138, Italy
[d] Department of Electronics, Information and Bioengineering, Politecnico di Milano, Via Giuseppe Ponzio 34, Milan, 20133, Italy
[e] Department of Engineering, Università degli Studi di Palermo, Viale delle Scienze Ed. 8, Palermo, 90128, Italy
[f] Department of Biomedical, Surgical and Dental Sciences, Università degli studi di Milano, Via della Commenda 10, Milan, 20122, Italy

HIGHLIGHTS

- Personalized flow rate boundary conditions using Echo Doppler data.
- Efficient Computational Fluid Dynamics after Transcatheter Aortic Valve Implantation.
- Influence of hemodynamics on the degeneration of transcatheter bio-prosthetic valves.
- Computational hemodynamic risk scores for Structural Valve Deterioration.

GRAPHICAL ABSTRACT

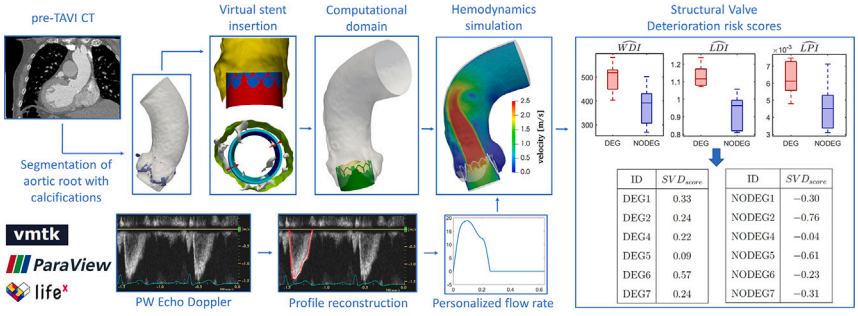

ARTICLE INFO

Keywords:
Transcatheter aortic valve implantation (TAVI)
Long-term durability
Structural valve deterioration (SVD)
Bio-prosthetic heart valves (BHV)
Computational fluid dynamics (CFD)
Patient-specific clinical data
Computational hemodynamic indices

ABSTRACT

Introduced as an alternative to open-heart surgery for elderly patients, Transcatheter Aortic Valve Implantation (TAVI) has recently been extended to younger patients due to comparable performance with the gold-standard. However, the long-term durability of the bio-prosthetic TAVI valves is limited by Structural Valve Deterioration (SVD), an inevitable degenerative process whose pathogenesis is still unclear. In this study, we aim to computationally investigate a possible relationship between aortic hemodynamics and SVD development. To this aim, we collect data from twelve patients with and without SVD at long-term follow-up exams. Starting from pre-operative clinical images, we build early post-operative virtual geometries and perform Computational Fluid Dynamics simulations by prescribing a personalized flow rate based on Echo Doppler data. In order to identify a premature onset of SVD, we propose three computational hemodynamic indices: Wall Damage Index (WDI), Leaflet Delamination Index (LDI), and Leaflet Permeability Index (LPI). Additionally, to each index we associate a score and, using the Wilcoxon rank-sum test, we find that each score individually shows a statistically greater median value in the SVD sub-population (WDI: $p = 0.008$, LDI: $p = 0.001$, LPI: $p = 0.020$). Finally, we define a synthetic scoring system that clearly separates between SVD and non-SVD patients. Our results suggest

* Corresponding author.
Email addresses: luca.crugnola@polimi.it (L. Crugnola), ccatalano@ismett.edu (C. Catalano), laura.fusini@cardiologicomonzino.it (L. Fusini), salvatore.pasta@unipa.it (S. Pasta), gianluca.pontone@cardiologicomonzino.it (G. Pontone), christian.vergara@polimi.it (C. Vergara).

https://doi.org/10.1016/j.compbiomed.2025.111435
Received 9 October 2025; Received in revised form 20 December 2025; Accepted 28 December 2025
Available online 5 January 2026

that aortic hemodynamics may drive a premature onset of SVD, and the synthetic score could potentially assist clinicians in a patient-specific planning of follow-up exams to closely monitor those patients at high SVD risk.

Glossary

TAVI	Transcatheter Aortic Valve Implantation
SVD	Structural Valve Deterioration
CFD	Computational Fluid Dynamics
CTA	Computed Tomography Angiography
PW	Pulsed Wave
TTE	Transthoracic Echocardiography
CW	Continuous Wave
LVOT	Left Ventricular Outflow Tract
NS	Navier-Stokes
LES	Large Eddy Simulation
RIIS	Resistive Immersed Implicit Surface
WSS	Wall Shear Stress
TAWSS	Time-Averaged Wall Shear Stress
OSI	Oscillatory Shear Index
TSVI	Topological Shear Variation Index
WDI	Wall Damage Index
LDI	Leaflet Delamination Index
LPI	Leaflet Permeability Index
ECAP	Endothelial Cell Activation Potential
RRT	Relative Residence Time
FSI	Fluid-Structure Interaction
PVL	Paravalvular Leakage
EOA	Effective Orifice Area
DVI	Doppler Velocity Index

1. Introduction

During the last two decades Transcatheter Aortic Valve Implantation (TAVI) has been established as a minimally invasive treatment for severe aortic stenosis in older patients at high-risk for open-heart surgery [1,2]. Thanks to the positive outcomes of recent clinical trials [3,4], nowadays TAVI represents the therapy of choice also for many lower-risk, younger patients [5]. In this context, it is particularly important to assess the long-term durability of the bio-prosthetic valves used for TAVI. Nonetheless, the relatively young age of this procedure, the limited life expectancy of its recipients, and the dispersion of patients after the intervention result in a lack of long-term follow-up data which makes it difficult to properly investigate the durability of TAVI valves.

The main limiting factor to the durability of bio-prosthetic valves is Structural Valve Deterioration (SVD), an intrinsic degenerative process manifested as permanent changes in the prosthesis, such as leaflet calcification or destruction of connective tissue, that ultimately leads to the failure of the implanted valves [5,6]. However, the pathogenesis of the SVD process is still incompletely understood and multiple mechanisms are thought to be involved [7]. Specifically, an elevated host cell infiltration was observed in explanted bio-prosthetic valves with SVD [8,9].

In the TAVI context, clinical studies have proposed several SVD risk factors that can be divided into valve-related and patient-related factors [10–12]. Some of these factors are associated to a high cardiac output and a small valvular orifice area. Accordingly, Ochi et al. hypothesized that an accelerated flow across the valve is a shared key component in the pathophysiology of SVD [13]. This suggests an influence of hemodynamics on the development of SVD.

To better investigate this point, in this paper we assess the role of hemodynamics in SVD by means of computational modeling, which represents a powerful tool to obtain a detailed quantitative description of blood-dynamics after TAVI. Within the TAVI framework, computational models have been extensively employed to simulate the deployment of the bio-prosthetic valve [14,15] and post-TAVI blood-dynamics [16,17], focusing on post-procedural complications such as paravalvular leakage [18,19], conduction abnormalities [20,21], and coronary obstruction [22]. Additionally, the durability of bio-prosthetic valves has been associated with the distribution of mechanical stresses in different device designs using computational mechanical models [23–25]. Moreover, a recent work experimentally showed that SVD is associated with mineral precipitation and cellular infiltration in the bio-prosthetic leaflets and the authors proposed computational hemodynamic indices that correlate with their findings in idealized geometries [26]. However, to the best of our knowledge, the only computational hemodynamic studies investigating the relationship between aortic hemodynamics and SVD using patient-specific clinical data have been carried out in our previous studies [27,28].

In this work we expand the analyses of [27,28] by further refining and personalizing the Computational Fluid Dynamics (CFD) model. In particular, the advancements of this paper rely on the introduction of a wire-frame description of the bio-prosthetic valve's stent, the modeling of the opening/closure dynamics of the valve's leaflets, the use of realistic TAVI leaflets geometry, and the flow rate conditions derived from Echo Doppler data.

The aims of this retrospective computational study are to:

1. Propose a framework to numerically simulate highly personalized post-TAVI hemodynamics starting from pre-operative clinical images and early post-operative Echo Doppler data;
2. Identify new hemodynamic indices in early post-TAVI virtual scenarios, i.e. when the implanted valve has not degenerated yet, that correlate with a premature onset of SVD, detected at 5–10 years follow-up exam.

2. Materials and methods

2.1. Clinical data

In this study we leverage clinical data related to twelve patients who underwent the TAVI procedure in Centro Cardiologico Monzino between 2008 and 2012. In each patient it was implanted an Edwards SAPIEN valve of either the first or second generation with a nominal size of 23 mm in external diameter. These are trileaflet bio-prosthetic valves made of bovine pericardium mounted on a balloon-expandable cylindrical stent with an inner fabric skirt on its ventricular side [29].

Six patients with SVD at long-term follow-up were identified and six patients without SVD at the same exam were randomly extracted from the same cohort and matched for baseline characteristics. We will refer to the former group as DEG patients and to the latter group as NODEG patients. In particular, the definition of SVD adopted in this paper is in agreement with both the "stage 3 SVD" definition proposed by Dvir et al. in [30] and the definition of SVD with "Stage 3 Hemodynamic Valve Deterioration" proposed by the Valve Academic Research Consortium (VARC) 3 in [31]. This means that all DEG patients satisfy the corresponding criteria as highlighted in Appendix A.

For each patient we have at our disposal the following data that we use as input in our model:

Table 1
Patients' characteristics in the study population. SAPIEN: type of SAPIEN valve. age: age at the time of TAVI. BSA: Body surface area. CO: cardiac output.

ID	SAPIEN	age	sex	BSA [m^2]	CO [$L/\min$]	native valve
DEG1	1st gen.	70	F	1.712	5.94	tricuspid
DEG2	2nd gen.	87	F	1.599	6.13	tricuspid
DEG4	2nd gen.	86	F	1.761	4.84	tricuspid
DEG5	1st gen.	75	F	2.062	5.45	tricuspid
DEG6	1st gen.	66	M	1.885	5.95	tricuspid
DEG7	2nd gen.	77	F	1.678	5.31	tricuspid
NODEG1	2nd gen.	87	F	1.504	5.37	tricuspid
NODEG2	2nd gen.	77	F	1.349	4.52	tricuspid
NODEG4	1st gen.	84	F	1.533	5.08	tricuspid
NODEG5	2nd gen.	66	F	1.593	4.37	tricuspid
NODEG6	2nd gen.	80	F	1.663	6.03	tricuspid
NODEG7	2nd gen.	86	F	1.787	5.94	tricuspid

1. Pre-TAVI Computed Tomography Angiography (CTA) scan. This is used in our model to reconstruct the patient-specific aortic geometries (see Section 2.2). See [11,27] for details on the CTA acquisition;
2. Early post-TAVI Pulsed Wave (PW) Doppler Transthoracic Echocardiography (TTE) data obtained between two days and seven months after the implantation. We exploit these data to derive a personalized flow rate profile that we impose as boundary condition in the numerical simulations (see Sections 2.3 and 2.4). See [11,27] for details on the Doppler TTE acquisition;
3. Long-term follow-up Doppler TTE data obtained 5–10 years after TAVI. These data are used to identify which patients developed SVD. The acquisition details are the same as in the previous point.

Moreover, for eleven out of twelve patients we have at disposal early post-TAVI maximum blood velocity measurements through the bio-prosthetic aortic valve taken from Continuous Wave (CW) Doppler TTE data that we use to validate the numerical hemodynamic results.

We report in Table 1 the patients' characteristics in our study population.[1] In particular, on average, DEG patients are characterized by: age $= 76.8$, BSA $= 1.783\,\mathrm{m}^2$, and CO $= 5.60\,L/\min$. Whereas, on average, NODEG patients are characterized by: age $= 80.0$, BSA $= 1.572\,\mathrm{m}^2$, and CO $= 5.22\,L/\min$.

The study was approved from IRB of Centro Cardiologico Monzino and registered with the number R.1262/20-CCM 1326.

2.2. Post-operative virtual geometries

We aim to perform a personalized computational analysis of post-TAVI hemodynamics exploiting the available clinical data (Section 2.1), so that we build early post-TAVI virtual geometries starting from pre-TAVI CTA scans. This procedure is extensively based on the use of the *Vascular Modeling Toolkit* (*VMTK*) [32] and *Paraview* open-source software and was already presented in [27,28]. In the following we give a brief overview of the procedure, detailing the advancements introduced in this study.

Pre-operative patient-specific geometries of the aortic root, the ascending aorta and the aortic valve's calcium deposits are semi-automatically reconstructed. The reconstructed aortic root geometry is then possibly deformed to be able to host the bio-prosthetic valve model, coherently with what happens during the balloon inflation step of the TAVI procedure. A cylindrical model of the SAPIEN valve's stent is oriented according to the aortic root centerline, centered in the aortic annulus barycenter and virtually inserted to be 70% in the aorta and 30% in the ventricle, according to clinical practice. Additionally, the cylindrical stent model is radially translated to account for the patient's calcification pattern. All the previous steps are detailed in [28]. Moreover, the virtual stent insertion procedure was qualitatively validated in [27] for two patients with available CTA scans taken few years after the TAVI intervention.

Regarding the stent model, an advancement of this work with respect to [27,28] is the introduction of a wire-frame design on the aortic side of the stent. Notice that the ventricular side of the stent is modeled as a hollow cylinder due to the presence of the inner skirt in the SAPIEN valves (see Fig. 1 left). Specifically, we generate realistic CAD models of the SAPIEN valves' stent with *SolidWorks* and *Autodesk Fusion* (Fig. 1 center). Then, starting from a hollow cylinder, we manipulate its geometry to match the wire-frame design of the CAD model only on the aortic side (Fig. 1 right).

As for the bio-prosthetic leaflets, two advancements with respect to [27,28] are the use of a realistic geometry, which mimics the SAPIEN valves' leaflets [34] (Fig. 2), and the modeling of the opening and closure dynamics. An open and a closed configuration of the leaflets are obtained with a mechanical simulation in *Abaqus*. Specifically, the leaflets are initially modeled in a stress-free configuration. A physiological pressure waveform is then applied to the leaflet surfaces, while the leaflet-to-stent attachment region is fully constrained. Following the simulation of an entire cardiac beat, the fully open and closed configurations of the bioprosthetic valve leaflets are exported as STL files for the subsequent step of the workflow. Then, we compute a distance from the closed to the open configuration and we use it to describe the opening and closure dynamics (see Section 2.4). Finally, the leaflet geometry is inserted into the stent model so that it has the same orientation of the stent and it is consistent with its wire-frame design.

The resulting computational domain, depicted in Fig. 3(a), has one inlet and one outlet sections. Additionally, the external wall comprises the interface between blood and the stent, the interface between blood and the native annulus, and the aortic wall.

As a last step we generate the computational mesh made of tetrahedral elements which are finer close to the inlet and coarser as they extend toward the outlet. On the whole aortic wall we consider a boundary layer made of three sub-layers with thicknesses $\{0.1,\ 0.2,\ 0.4\}\,\mathrm{mm}$ going from the wall to the internal domain. Moreover, we refine the mesh to a $0.25\,\mathrm{mm}$ size in the leaflets area to ensure a proper implicit representation of the leaflets in the numerical simulations (see Section 2.4). The resulting mesh (see Fig. 3b) has an average size of $\approx 0.8\,\mathrm{mm}$ and is chosen after a mesh sensitivity analysis (see Appendix B).

2.3. Personalized flow rate profile

In accordance with [27], we want to prescribe a flow rate condition at the inlet section of the computational domain (Fig. 3a). In particular, in [27] a physiological flow rate profile was taken from the literature [36] and its magnitude was scaled to match the patient's cardiac output. In order to further personalize our CFD model, in this work we assume that the inlet flow rate shares the same temporal evolution profile as the blood velocity inside the Left Ventricular Outlet Tract (LVOT), reconstructed from the available PW Doppler TTE image. The resulting flow rate is characterized by a patient-specific mean value (i.e. cardiac output), heart rate, and partition between the systolic and diastolic phase.

More specifically, PW Doppler TTE images show the temporal evolution of the blood velocity at the center of the LVOT during a few heartbeats. For each heartbeat, we manually draw the velocity temporal evolution during systole, following the Doppler signal's contour and the drawings performed by clinicians, if present. These manual drawings were validated by an expert clinician for the whole study population.

[1] Notice that the twelve patients of our study population come from a larger cohort of fourteen patients analyzed in [27]. In particular, patients DEG3 and NODEG3 are missing in this study due to the unavailability, for these two patients, of the early post-TAVI PW Doppler TTE data used to derive the inlet boundary condition in our model.

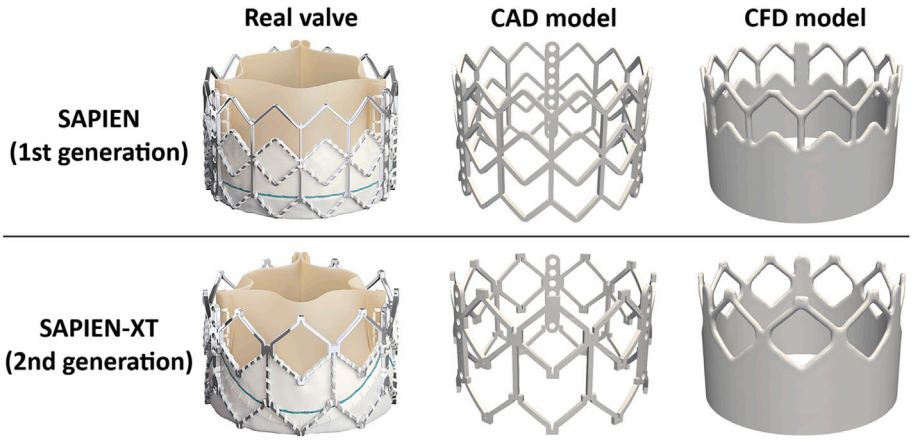

Fig. 1. For each SAPIEN valve considered in this study, we report: an image of the real valve (left), the CAD model (center) and the stent model used in the CFD simulations (right). The "Real valve" images are taken from Rheude, Blumenstein, Möllmann, Husser [33] under CC-BY-NC license, ©Edwards Lifensciences Corporation.

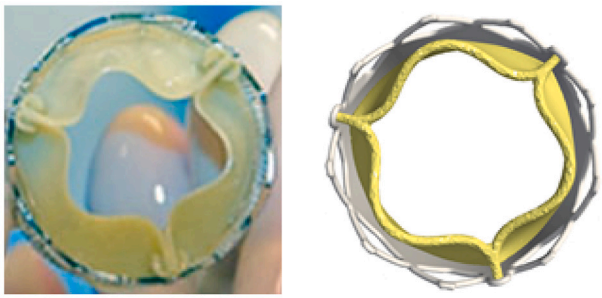

Fig. 2. SAPIEN leaflets in open configuration: image of the real valve (a) and model used in the CFD simulations (b). The image of the real valve is taken from Holoshitz, Kavinsky, Hijazi [35] with written permission by Hijazi.

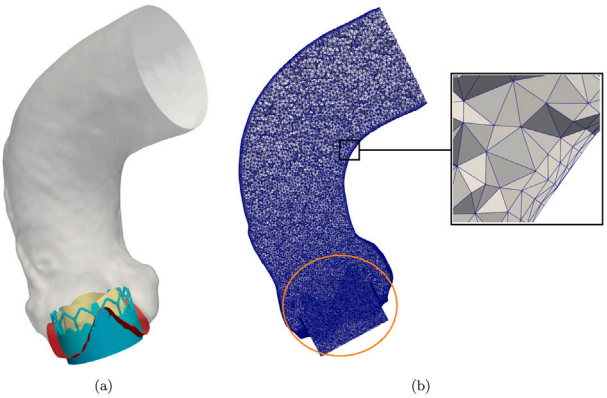

Fig. 3. (a) Computational domain comprising the interface between blood and the stent (light blue), the interface between blood and the native annulus (red), the aortic wall (gray), and the leaflets geometry (yellow). (b) Volumetric computational mesh with a boundary layer (zoom in black box) and a local refinement in the leaflet area (highlighted in orange).

Then, using *WebPlotDigitizer*, we digitize the drawn profiles and we identify the end of the heartbeat. In particular, the end of the heartbeat is identified by exploiting the electrocardiography signal, available in the image, and the start of the velocity signal of the following heartbeat. Finally, we average the digitized signals between the heartbeats and we scale the averaged profile to match the patient-specific cardiac output and heart rate. The full procedure is schematized in Fig. 4.

Let us notice that, in the clinical setting, the cardiac output is usually computed from PW Doppler TTE data assuming a flat velocity profile in the LVOT. This tends to overestimate the real cardiac output by about 15% [37] due to the skewness of the real velocity profile. Accordingly, in this work we rescale the clinical cardiac outputs reported in Table 1 so as to eliminate this overestimation (for simplicity assumed to be equal to 15% in all the patients).

2.4. Mathematical and numerical modeling

In this work we considered the same mathematical model presented in [27], where the system of equations is reported. In particular, we model blood as an incompressible homogeneous Newtonian fluid, with a density of $1060\,\mathrm{kg/m^3}$ and a dynamic viscosity of $3.5\times10^{-3}\ Pa\cdot s$ [38], using the Navier-Stokes (NS) equations, as commonly done in large vessel like the aorta [39,40]. We account for the presence of turbulence in the ascending aorta [41] by employing a Large Eddy Simulation (LES) method, which is most suitable due to its capability to capture the laminar, transitional and turbulent features characterizing the cardiac cycle [42]. Specifically, we use the LES σ-model [43], which has proven to perform well in closed channel configurations, showing accurate results in the near wall region [44]. We provide an implicit representation of the bio-prosthetic leaflets with the Resistive Immersed Implicit Surface (RIIS) method [45]. This method adds to the NS momentum equation a local penalization term which surrogates the obstruction to the flow caused by the presence of the leaflets. As for the boundary conditions, we consider the external wall as rigid (CFD approach), we impose a physiological pressure at the outlet section and a flow rate condition, prescribing the personalized flow rate profile presented in Section 2.3, at the inlet section. The latter condition does not provide enough information to close the NS problem, thus it needs to be completed. In order not to set a priori a spatial profile for the velocity field at the inlet, which would affect the accuracy of the numerical solution [46], we prescribe this condition using a Lagrange multiplier [47]. This approach assumes the fluid traction to be normally directed and constant at the inlet section and results in an augmented formulation of the NS systems. In particular, the Lagrange multiplier method for the prescription of a flow rate condition has been shown to perfectly match a Womersley profile in the case of pulsatile flow in a cylinder [46].

Regarding the modeling of the leaflets opening and closure dynamics, in the numerical simulations we use the distance function introduced in Section 2.2 to interpolate between the closed and open configurations of the leaflets, according to the following law: the opening and closure

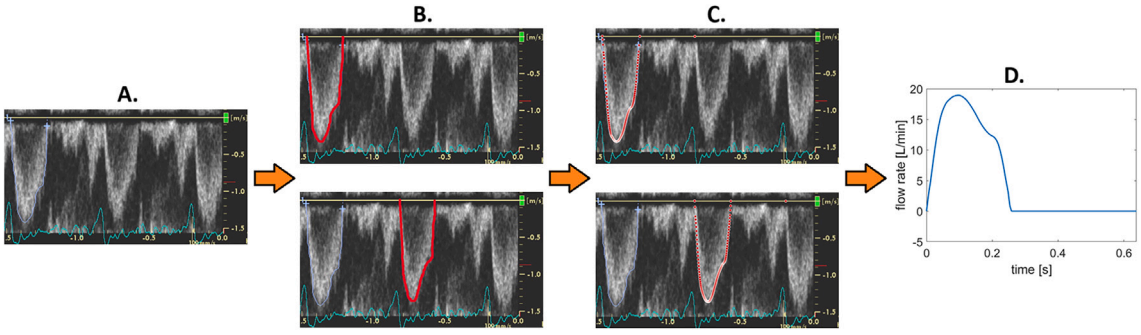

Fig. 4. Derivation of the personalized flow rate profile. Starting from a PW Doppler TTE image (A.), we manually draw the temporal evolution of the blood velocity during systole for each visible heartbeat (B.), we digitalize each drawing and identify the end of the heartbeat (C.), we average the digitalized profiles between the heartbeats and we rescale the averaged profile to match the patient's cardiac output and heart rate (D.).

times are 15 ms and 45 ms, respectively, according to [48,49]; moreover, the transition between the two configurations is regulated by a valve opening coefficient which follows the cosine-exponential ramps

$$r(t) = \begin{cases} r_{op}(t) = 0.5\left(1-\cos\left(\pi\left(\frac{1-e^{-p_{op}t}}{1-e^{-p_{op}}}\right)\right)\right) & \text{during opening,} \\ r_{cl}(t) = 1-0.5\left(1-\cos\left(\pi\left(\frac{1-e^{-p_{cl}t}}{1-e^{-p_{cl}}}\right)\right)\right) & \text{during closure,} \end{cases}$$

where t is a standardized time and $p = \{p_{op}, p_{cl}\}$ is a parameter to be calibrated for each phase. We vary $p_{op} \in [2.5, 3.5]$ for the opening ramp and $p_{cl} \in [-3, -2]$ for the closure ramp according to the slope of the input flow rate profile at the opening and closure instants. Specifically, patients showing steeper flow rate profiles are associated to higher absolute values of p. We stress that the leaflets geometry is a surface made of shell elements, we implicitly represent it as an immersed surface and provide a thickness to it directly in the numerical simulations using the RIIS method (see [27] for details).

Let us now present the numerical methods employed in this study. A spatial discretization of the problem is achieved using a Finite Element approach with piece-wise linear elements both for the velocity and pressure fields, referred to as P1-P1. A Streamline Upwind Petrov–Galerkin/Pressure Stabilizing Petrov–Galerkin (SUPG/PSPG) stabilization [50] is considered to account for the advection-dominated regime and the use of P1-P1 spaces, which are inf-sup unstable. Possible numerical instabilities arising from the presence of recirculating areas at the outlet section are addressed with a backflow stabilization [51]. Moreover, the problem is discretized in time with a first order backward Euler scheme with a semi-implicit treatment of the convective term and an explicit treatment of the sub-grid scale viscosity, introduced by the LES σ-model. We consider a different time-step for each patient according to the duration of the patient's systolic phase. Specifically, a time-step $\Delta t = 10^{-3}\ s$ is used for patient NODEG6 who shows the longest systolic period ($0.4\ s$) and for the other patients the time-step is scaled so that we have roughly the same number of time instants during systole. Finally, the augmented algebraic system arising from the introduction of a Lagrange multiplier to impose the inlet flow rate condition is monolithically solved using a preconditioned GMRES iterative solver [52], exploiting an ad-hoc preconditioner [53].

For the implementation of the mathematical and numerical methods presented in this subsection we rely on the multi-physics high-performance Finite Element library life^x [54,55], developed at MOX, Dipartimento di Matematica, with the collaboration of LaBS, Dipartimento di Chimica, Materiali ed Ingegneria Chimica (both at Politecnico di Milano).

2.5. Post-processing of the results

Due to the turbulent nature of the analyzed flow, in this paper we numerically simulate eight complete heartbeats, discarding the first two to avoid the influence of the null initial condition. In particular, using the *Paraview* software, we post-process the *phase-average* (also named as *ensemble*) velocity and pressure fields, i.e., the average at each time over the six heartbeats:

$$\phi(\boldsymbol{x}, t) = \frac{1}{6}\sum_{n=1}^{6} \phi^n(\boldsymbol{x}, t),$$

where ϕ^n is either the velocity or the pressure at the n-th heartbeat. Specifically, in this paper we aim to propose computational hemodynamic indices, obtained by the phase-average fields, in early post-TAVI scenarios that correlate with a premature onset of SVD, detected at 5-10 years follow-up exam.

2.5.1. Quantities of interest

Let us define the fluid viscous stress on a surface as:

$$\boldsymbol{\tau} = 2\mu\left(\frac{\nabla \boldsymbol{u} + \nabla^T \boldsymbol{u}}{2}\right)\boldsymbol{n}$$

where μ is the blood viscosity, $\boldsymbol{u}$ is the (phase-average) blood velocity and $\boldsymbol{n}$ is the surface normal. Accordingly, the Wall Shear Stress (WSS) vector reads:

$$\boldsymbol{\tau}_{WSS} = \boldsymbol{\tau} - (\boldsymbol{\tau}\cdot\boldsymbol{n})\boldsymbol{n},$$

which allows us to define the following quantities:

- Time-Averaged WSS ($TAWSS$):

$$TAWSS(\mathbf{x}; [T_1, T_2]) = \frac{1}{T_2 - T_1}\int_{T_1}^{T_2} ||\boldsymbol{\tau}_{WSS}||\, dt,$$

  where T_1 and T_2 identify the time-period (systole, diastole or complete heartbeat) which could change according to the index, and $||\boldsymbol{v}||$ is the magnitude of a generic vector $\boldsymbol{v}$;
- Oscillatory Shear Index (OSI):

$$OSI(\mathbf{x}; [T_1, T_2]) = \frac{1}{2}\left(1 - \frac{||\int_{T_1}^{T_2} \boldsymbol{\tau}_{WSS}\, dt||}{\int_{T_1}^{T_2} ||\boldsymbol{\tau}_{WSS}||\, dt}\right).$$

  It provides a measure of the oscillatory nature of the WSS vector;
- Topological Shear Variation Index ($TSVI$):

$$TSVI(\mathbf{x}; [T_1, T_2]) = \sqrt{\frac{1}{T_2 - T_1}\int_{T_1}^{T_2}\left(\nabla\cdot\boldsymbol{\tau}^N_{WSS} - \overline{\nabla\cdot\boldsymbol{\tau}^N_{WSS}}\right)^2 dt}$$

  where $\nabla\cdot$ is the divergence operator, $\boldsymbol{\tau}^N_{WSS} = \frac{\boldsymbol{\tau}_{WSS}}{||\boldsymbol{\tau}_{WSS}||}$ is the normalized WSS vector, and $\overline{\nabla\cdot\boldsymbol{\tau}^N_{WSS}} = \frac{1}{T_2 - T_1}\int_{T_1}^{T_2} \nabla\cdot\boldsymbol{\tau}^N_{WSS}\, dt$ is the average in time of the divergence of the normalized WSS vector. It represents the variation in the WSS action on the vessel expansion/contraction [56].

2.5.2. Hemodynamic indices and scores

SVD has been associated with an increased infiltration of host cells (e.g. immune cells, cell debris) in the bio-prosthetic leaflets [8,9,26]. Accordingly, we propose three computational hemodynamic indices in order to study their correlation with a premature onset of SVD.

A diffuse damage/inflammation of the aortic wall can lead to the recruitment of immune cells to the aortic root [57], thus facilitating their infiltration in the leaflets. To quantify this damage we propose the Wall Damage Index (WDI) computed on the aortic wall:

$$WDI(\mathbf{x}) = TAWSS(\mathbf{x};[0;T]) \times TSVI(\mathbf{x};[0;T])$$

where T is the duration of the whole heartbeat. It is known that high WSS, here associated with high $TAWSS$ values, on the vessel wall can result in endothelial changes, possibly promoting inflammation [58]. Additionally, significant variations in WSS directionality, corresponding to high $TSVI$ values, can affect vascular diseases by influencing endothelial cells [59]. Thus, we associate high WDI values with a possible damage of the aortic wall.

High stresses on the bio-prosthetic leaflets can cause the delamination of the connective tissue, promoting the infiltration of immune cells [7]. For this reason, we propose the Leaflet Delamination Index (LDI) computed on the ventricular side of the leaflets:

$$LDI(\mathbf{x}) = TAWSS(\mathbf{x};[0;T_S])$$

where T_S is the systolic end instant.

Low and oscillatory WSS is known to impair endothelial integrity, thus increasing its permeability [60]. Accordingly, we propose the Leaflet Permeability Index (LPI) computed on the aortic side of the leaflets:

$$LPI(\mathbf{x}) = OSI(\mathbf{x};[T_S;T]) \times \left(0.05 - TAWSS(\mathbf{x};[T_S;T])\right).$$

Notice that, high OSI and low $TAWSS$ values result in high LPI values.

To investigate the correlation between the proposed indices and the premature onset of SVD, we define a hemodynamic score associated with each index by spatially averaging the index on the corresponding surface. Specifically, WDI is averaged on the whole aortic wall to obtain $\widehat{WDI}$, LDI is averaged on the ventricular side of the leaflets to obtain $\widehat{LDI}$, and LPI is averaged on the aortic side of the leaflets to obtain $\widehat{LPI}$.

2.5.3. Synthetic score

With the aim of clearly separating between patients with and without SVD at the long-term follow-up exam (DEG vs NODEG), we define a global synthetic score, which combines the proposed hemodynamic scores.

In order to be combined, the hemodynamic scores have to first be standardized. To do so, similarly to [27], we compute the $25th$ percentile (Q_1), the $75th$ percentile (Q_3), and the inter-quartile range ($IQR = Q_3 - Q_1$) for each hemodynamic score in the whole study population and we linearly project the interval $[Q_1 - IQR, Q_3 + IQR]$ into the interval $[-1, 1]$. The standardization procedure is performed using the *Matlab* software.

The global synthetic score SVD_{score} reads:

$$SVD_{score} = \frac{(\widehat{WDI}_S + \widehat{LDI}_S + \widehat{LPI}_S)}{3},$$

where the subscript S denotes the hemodynamic standardized score.

2.5.4. Validation of the numerical results

To validate the numerical results of our CFD model we use the maximum blood velocity measurements through the bio-prosthetic valve taken from early post-TAVI CW Doppler TTE data, available for all patients in the study population (apart from DEG2). During CW Doppler TTE a transducer continuously transmits ultrasound waves and receives echoes in order to measure blood velocities along an entire beam Γ oriented as the valve and passing through its center. The maximum blood velocity through the valve is identified as the maximum velocity magnitude obtained along the beam Γ during the heartbeat, and we compare it with the same quantity extracted from the CFD results, assuming a Doppler-like beam Γ with a radius of 1 mm. We report in Table 2-right an example of the beam Γ, for both the Doppler and CFD measures.

Table 2
Left: Numerical blood velocity validation for the eleven patients with available clinical datum (all but DEG2). Early post-TAVI maximum blood velocity magnitude through the bio-prosthetic valve taken from CW Doppler TTE data ($V_{max}^{Doppler}$) and from the CFD results (V_{max}^{CFD}), and relative error between the two measures (Err). The error range is computed accounting for the decimal truncation of $V_{max}^{Doppler}$ (i.e. $\pm 0.05\,[\frac{m}{s}]$). Right: Visualization of the Doppler image and an example of the region Γ where the maximum blood velocity magnitude is computed from the CFD results.

ID	$V_{max}^{Doppler}\,[\frac{m}{s}]$	$V_{max}^{CFD}\,[\frac{m}{s}]$	$Err\,[\%]$
DEG1	2.6	2.92	10.6–14.5
DEG4	2.6	2.51	1.6–4.9
DEG5	2.5	2.33	4.9–8.2
DEG6	2.6	2.62	0.0–2.7
DEG7	2.4	2.39	0.0–2.0
NODEG1	2.5	2.54	0.0–3.7
NODEG2	2.0	2.04	0.0–4.6
NODEG4	2.5	2.51	0.0–2.4
NODEG5	2.3	1.85	17.8–20.9
NODEG6	2.1	2.29	7.0–11.7
NODEG7	2.5	2.08	15.1–18.1

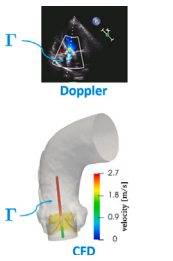

3. Results

All the numerical simulations were run in parallel on 112 cores of Intel Sapphire Rapids@2.00GHz CPUs, using the computational resources provided by the CINECA supercomputing center, Italy. The average computational time for each simulation (i.e. for eight complete heartbeats) is 17.0 ± 5.3 hrs.

3.1. Outcomes of the validation of the numerical results

In Table 2 we report the maximum blood velocity obtained from CW Doppler TTE and from the CFD results (see Section 2.5.4). Out of the eleven patients with available clinical datum, the table shows that: in four patients (DEG6, DEG7, NODEG1, NODEG4) the agreement is excellent and the error is very close to zero; in two patients (DEG4, NODEG2) there is a very slight increase in the error, which however is less than 5%; in another two patients (DEG5, NODEG6) we have a good agreement with errors around 10%; in the remaining three patients (DEG1, NODEG5, NODEG7) we experienced increased errors up to 20%.

3.2. Analysis of the hemodynamic patterns

In the following we analyze the CFD results for patient DEG1, as a representative of the study population.

In Fig. 5 we report, for three selected instants during systole,[2] the CFD velocity streamlines on both a longitudinal and a cross-section plane, the pressure on a longitudinal plane, and the WSS magnitude patterns on the aortic wall. From the velocity plots we can observe that the presence of a small size TAVI valve (23 mm in external diameter) gives rise to the a high-velocity jet forming across the implanted valve, together with some vortical structures along side the jet (early systole). Let us note that, the velocity magnitude obtained inside the jet

[2] Notice that such values could be slightly different among patients according to the duration of the corresponding heartbeat.

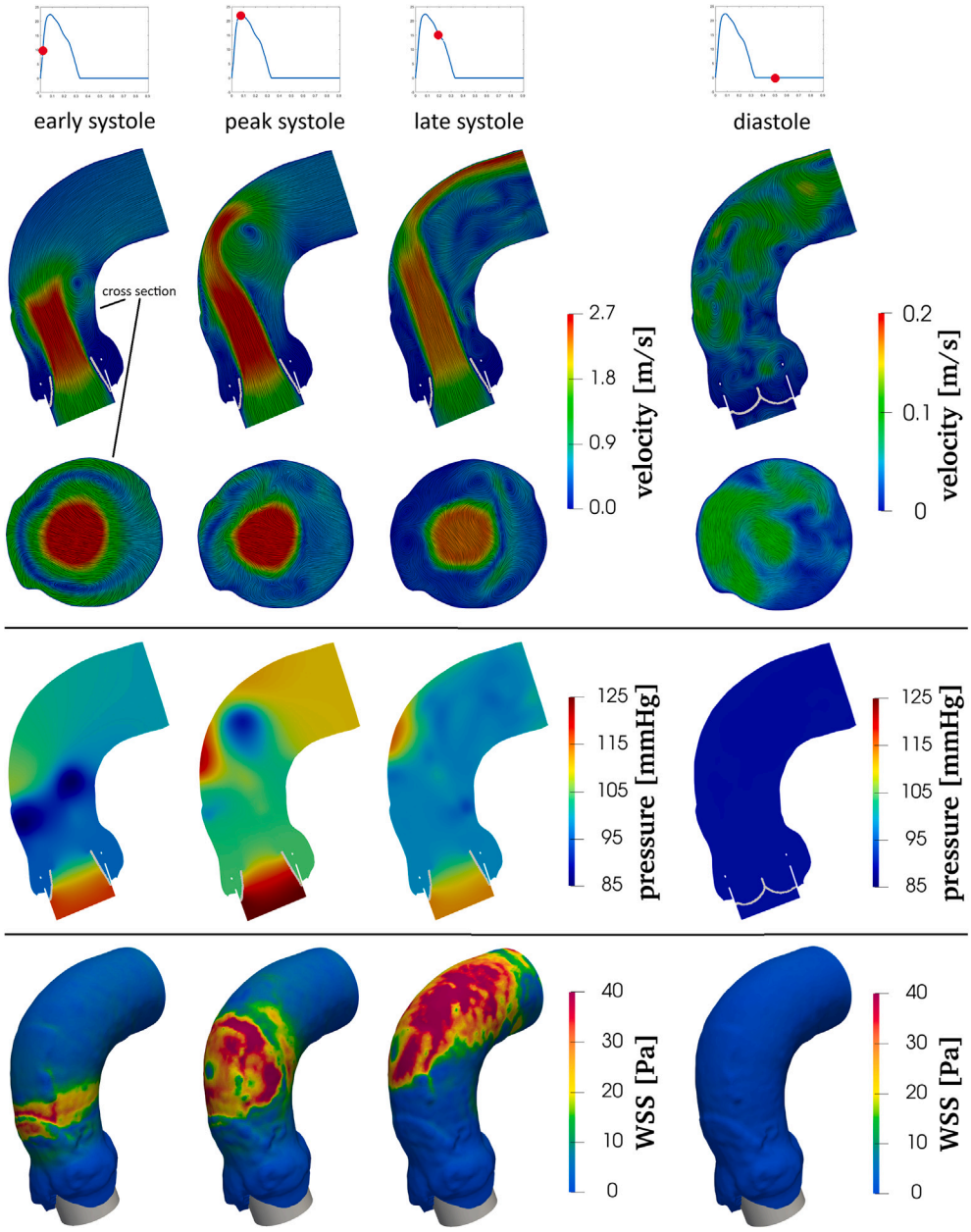

Fig. 5. Evolution of the velocity streamlines on both a longitudinal and a cross-section plane (top), of the pressure on a longitudinal plane (middle), and of the WSS magnitude on the the aortic wall (bottom) at three selected instants during systole and one during diastole (for the represented patient DEG1, they are t = 0.063 s, t = 0.093 s, t = 0.159 s, t = 0.489 s). Notice that, for visualization purposes, we used a different scale for the velocity plots during the diastolic instant.

strictly depends on the personalized flow rate profile (see Section 2.3) prescribed at the inlet, since the geometric opening area of the valve is the same for each patient in our model. The impingement of the vortices on the aortic wall (peak systole) results in very chaotic hemodynamic patterns with recirculating areas in the ascending aorta (late systole, diastole). Thus, our model is able to capture the secondary vortical flow structures which characterize the aortic arch hemodynamics [61,62]. Additionally, the accelerated flow results in significant pressure gradients across the valve, with maximum values around $20\,[mmHg]$. In particular, in the first two time instants, low pressure values are obtained near the vortices inside the ascending aorta, with a pressure recovery towards the outlet section. Furthermore, high WSS magnitudes are obtained on the aortic wall due to the collision of the jet on the wall.

In Fig. 6 we report the spatial distribution of the hemodynamic indices presented in Section 2.5.2, which is driven by the complex hemodynamics described above. Indeed, the high stresses on the aortic wall and the disturbed flow patterns, leading to significant topological variations of the WSS vectors, are the main determinants for the WDI distribution. Furthermore, the accelerated flow across the valve affects the stress intensity on the ventricular side of the leaflets during systole, thus influencing the LDI. Finally, the chaotic flow patterns, characterized by several vortical structures in the aorta, leads to low and oscillatory stresses on the aortic side of the leaflets during diastole, thus influencing the LPI intensity and patterns.

3.3. Hemodynamic and synthetic scores

In Table 3 we report the values of each hemodynamic score, defined in Section 2.5.2, in the study population. From the table it is clear that different scores take value in significantly different ranges, thus stressing the importance of the standardization procedure, described in Section 2.5.3, in order to combine them.

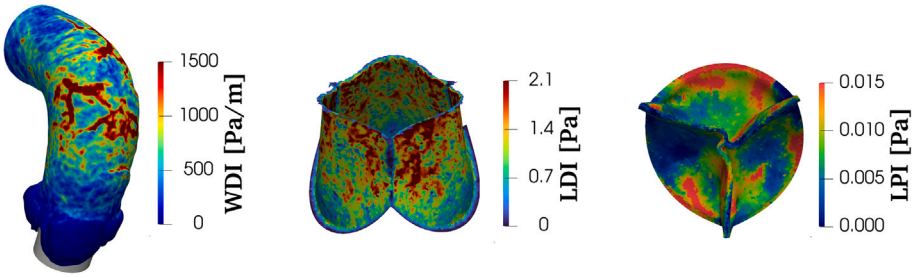

Fig. 6. Hemodynamic indices WDI, LDI and LPI (see Section 2.5.2). Patient DEG1.

Table 3
For each patient in the study population we report the values of the hemodynamic scores $\widehat{WDI}$, $\widehat{LDI}$ and $\widehat{LPI}$ defined in Section 2.5.2.

ID	$\widehat{WDI}\ \left[\frac{Pa}{m}\right]$	$\widehat{LDI}\ [Pa]$	$\widehat{LPI}\ [Pa]$
DEG1	5.10×10^2	1.08×10^0	7.27×10^{-3}
DEG2	5.31×10^2	1.12×10^0	5.58×10^{-3}
DEG4	4.03×10^2	1.12×10^0	7.49×10^{-3}
DEG5	5.28×10^2	1.07×10^0	4.81×10^{-3}
DEG6	5.83×10^2	1.24×10^0	6.11×10^{-3}
DEG7	4.50×10^2	1.17×10^0	6.14×10^{-3}
NODEG1	3.98×10^2	1.06×10^0	3.36×10^{-3}
NODEG2	2.69×10^2	0.81×10^0	4.64×10^{-3}
NODEG4	3.85×10^2	0.98×10^0	7.14×10^{-3}
NODEG5	3.07×10^2	0.82×10^0	5.29×10^{-3}
NODEG6	4.31×10^2	0.99×10^0	4.39×10^{-3}
NODEG7	5.03×10^2	0.95×10^0	3.11×10^{-3}

Table 4
For each patient in the study population we report the value of the global synthetic score SVD_{score} defined in Section 2.5.3.

ID	SVD_{score}
DEG1	0.33
DEG2	0.24
DEG4	0.22
DEG5	0.09
DEG6	0.57
DEG7	0.24
NODEG1	−0.30
NODEG2	−0.76
NODEG4	−0.04
NODEG5	−0.61
NODEG6	−0.23
NODEG7	−0.31

In Fig. 7 we plot the hemodynamic scores distributions in the DEG and NODEG sub-populations using boxplots. The figure shows that each score tends to be characterized by greater values for DEG patients with respect to NODEG patients. In order to properly assess the observed trend, for each individual hemodynamic score we employ, using *Matlab*, a right-tailed Wilcoxon rank-sum test having as alternative hypothesis that the median of the DEG distribution is statistically greater than the median of the NODEG distribution. This non-parametric test is chosen due to the limited number of observations. The p-values resulting from these tests are: $p = 0.0076$ for $\widehat{WDI}$, $p = 0.0011$ for $\widehat{LDI}$, and $p = 0.0206$ for $\widehat{LPI}$. Thus, with respect to each hemodynamic score the DEG distribution is statistically greater than the NODEG distribution at a 2.5% significance level. Lastly, in Table 4 we report the values of the global synthetic score SVD_{score}, defined in Section 2.5.3, in the entire study population. The SVD_{score} is able to clearly separate between the two sub-populations, with each DEG patient showing positive values and each NODEG patient showing negative values of this score.

4. Discussion

The mechanisms underlying the development of SVD in transcatheter bio-prosthetic valves are still not fully understood: multiple active processes are involved, from mechanical stresses to long-term immune rejection and atherosclerosis-like tissue remodeling [7]. Specifically, inflammatory reaction and immune response may play a crucial role in the pathogenesis of SVD, which is associated with an elevated immune cell infiltration in the bio-prosthetic leaflets [8,9]. Clinical studies identified some risk factors related to SVD, such as small prosthesis size [11], a valve-in-valve procedure [10], young age, patient-prosthesis mismatch, larger body surface area, and smoking [12]. Also, in [13] the authors hypothesized that an accelerated flow across the implanted valve, due

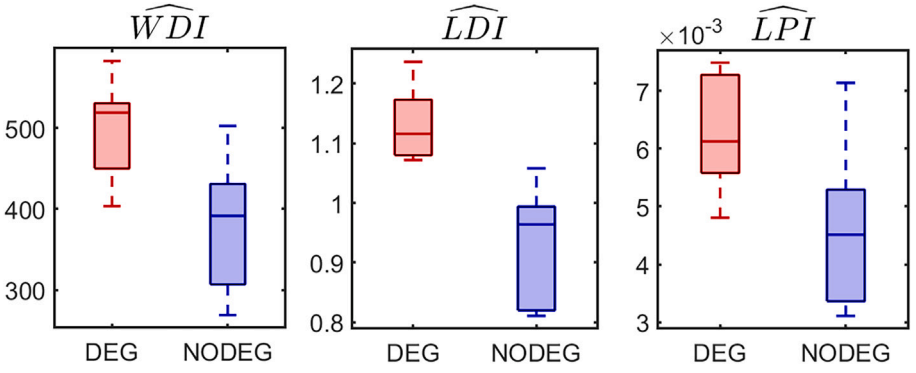

Fig. 7. Boxplot distributions of each hemodynamic score in the DEG and NODEG sub-populations.

to a high cardiac output, could be a factor in the development of SVD. This is in agreement with the characteristics of our study population (see Table 1) which shows that, on average, DEG patients are younger, with a larger body surface area, and with an increased cardiac output. However, the risk factors reported in Table 1 alone are not able to discriminate between DEG and NODEG patients.

In this context, computational modeling represents a powerful tool for filling the gap by identifying the conditions that may lead to a premature onset of SVD. Indeed, it provides a detailed description of post-TAVI hemodynamics, allowing for the investigation of the accelerated flow features that may influence SVD.

Accordingly, in this study we introduced new hemodynamic computational risk factors for the premature onset of SVD. Specifically, we proposed three hemodynamic scores ($\widehat{WDI}$, $\widehat{LDI}$, and $\widehat{LPI}$), that can be related to an infiltration of host cells in the bio-prosthetic valve leaflets (see Section 2.5.2), and a global synthetic score (SVD_{score}) which combines such scores (see Section 2.5.3). This is done by numerically simulating early post-TAVI hemodynamics in a cohort of patients for which a follow-up at 5-10 years is available.

First, we notice that in our study we analyzed post-TAVI hemodynamics just after the implantation. This is based on the assumption that the hemodynamic patterns initiating the development of SVD are influential already a short time after the intervention [30], when the implanted bio-prosthetic valve is still fully functioning. This allowed us to avoid the modeling of the bio-prosthetic leaflets degeneration process.

Moreover, we focused on balloon-expandable TAVI valves with a very similar design, i.e. the Edwards SAPIEN and SAPIEN-XT 23 *mm* valves (referred to as Edwards SAPIEN 23 *mm* in the following, for simplicity). This was done since we only had at disposal clinical data related to DEG patients who received an Edwards SAPIEN 23 *mm* valve. Accordingly, in order to build significant hemodynamic scores discriminating between DEG and NODEG patients, we considered also for the latter group Edwards SAPIEN 23 *mm* cases.

Regarding the personalized flow rate profile (Section 2.3) prescribed in the numerical simulations at the inlet, we assumed that it shares the same temporal trend of the blood velocity in the LVOT, measured for the patient by Echo Doppler. The accuracy of this assumption depends on the skewness of the velocity profile, which is not known. However, the phase discrepancy between the two signals is expected to be small, and this strategy is anyway patient-specific, thus more accurate than considering a flow rate taken from the literature, as done for example in [27].

In the literature, combinations of $TAWSS$ and OSI to identify vessels regions subject to low and oscillatory shear stresses are commonly based on the use of the Endothelial Cell Activation Potential ($ECAP$) [63,64] and Relative Residence Time (RRT) [65], which depend on the inverse of $TAWSS$. Our numerical results are often characterized by values of $TAWSS \approx 0$ in some very localized areas of the leaflets during diastole, leading to very high $ECAP$ and RRT values that would dominate over the spatial average needed to the define the hemodynamic score. For this reason, in this study we proposed LPI which does not have a singularity for $TAWSS = 0$ (Section 2.5.2).

Doppler-based blood velocity measurements showed a variability up to 9% between different measurements performed by the same experienced vascular technologist in an idealized in-vitro setting [66]. Accordingly, we found a good quantitative agreement between the CW Doppler TTE and CFD measures in the validation analysis reported in Section 3.1, with seven out eleven patients showing errors smaller than the 9% threshold, and patient NODEG6 showing errors around 10% (close to the threshold). The greater discrepancies observed for patients DEG1, NODEG5 and NODEG7 can be mainly due to two reasons: an under/over expansion of the real implanted TAVI valve, that we cannot model since we do not have at our disposal any intra-procedural data; or an inaccurate computation of the personalized flow rate profile, due to a mismatch between the flow rate and blood velocity temporal trends for these patients or a sub-optimal reconstruction of the velocity temporal profile from the PW Doppler TTE image.

The analysis of the computational hemodynamic patterns (Section 3.2) highlighted the mildly stenotic scenario that follows the implantation of a balloon-expandable, small size TAVI valve (Edwards SAPIEN 23 mm), characterized by high velocity magnitudes and a pressure recovery distal to the aortic valve [67]. This is consistent with the observation that all stented bio-prosthetic valves result in a residual stenosis of up to 20% [68]. Specifically, the formation of a high-velocity jet in the ascending aorta leads to complex and disturbed hemodynamic patterns possibly speeding up SVD pathogenesis through inflammatory reactions and infiltration of host cells in the leaflets.

We identified three hemodynamic indices in early post-TAVI scenarios that showed statistically significant differences between patients, who received an Edwards SAPIEN 23 mm valve, with and without SVD at long-term follow-up exam (see Section 3.3). This is a very promising result showing that patients with a prematurely degenerated valve belong to a different statistical distribution with respect to the considered hemodynamic features even when the valve is not degenerated yet. Therefore, this analysis represents a preliminary proof of the influence of aortic hemodynamics on the development of SVD, which should be considered for a proper assessment of SVD and has been rarely investigated with computational models.

The definition of the global synthetic score SVD_{score} allowed us to obtain a scoring system capable of clearly separating patients, who received an Edwards SAPIEN 23 mm valve, with and without SVD in view of a possible clinical translation (see Table 4). We found that the global score is more robust than the three individual hemodynamic scores, probably because it takes into account multiple mechanisms facilitating immune cells infiltration (aortic wall damage/inflammation, leaflet delamination, leaflet increased permeability). Additionally, we notice that also the individual $\widehat{LDI}$ score alone is also able to separate the two sub-populations (see Fig. 7-middle), even if with a less evident separation (0.13 for SVD_{score}, see Table 4, vs 0.06 for the standardized $\widehat{LDI}_S$, not reported here for the sake of exposition).

The proposed synthetic SVD_{score} could be easily translated into clinical practice to identify, early after the intervention, those patients, with an Edwards SAPIEN 23 mm valve, who are at higher risk of a premature onset of SVD. This could drive a patient-specific planning of follow-up exams to closely monitor the high SVD risk patients, trying to avoid their dispersion after the procedure.

Lastly, we notice that the clinical data needed to build the proposed scores (pre-TAVI CTA scans and early post-TAVI Doppler TTE measures) are routinely acquired within the TAVI context. Since the model does not require any ad-hoc or invasive clinical measurements, our framework can be used to perform both prospective and retrospective studies, providing a detailed and personalized description of the main flow features while sparing patients from additional measurements and exams.

5. Limitations

We start by noticing that our mathematical and numerical model (Section 2.4) is characterized by some simplifications:

1) We modeled blood as a homogeneous Newtonian fluid and the wall as rigid. This can have an influence on hemodynamic features such as the Wall Shear Stress (WSS) [69]. However, we notice that we study elderly patients which are usually characterized by a limited tissue elasticity due to stiffening and calcifications. Moreover, in large vessel like the aorta, the influence of blood cells can be neglected and the Newtonian assumption is the standard one [70];
2) We did not account for the coronary branches and thus for the corresponding blood flow. This could affect blood-dynamics inside the aortic root, specially during diastole, and thus the hemodynamic indices proposed in Section 2.5.2, specially LPI, being computed during the diastolic phase. Notice that, considering coronary flow with a rigid aortic wall could lead to non-physiological flow patterns since the blood flowing to the coronaries is thought to come from

the relaxation of the aortic root wall following its systolic expansion [71]. In any case, we believe that the inclusion of the coronary flow should have a common effect on the hemodynamic quantities among patients;

3) We provided an implicit dynamic representation of the bio-prosthetic leaflets with the RIIS method. This allowed us to capture the main flow features, such as the opening/closure dynamics and a realistic opening area. However, a Fluid-Structure Interaction (FSI) approach should be able to represent complex features, such as leaflets fluttering, and results in a more accurate computation of the stresses on the leaflets, thus could be considered in future studies.

These simplifications significantly reduced the computational cost of the numerical simulations to make our model suitable to analyze a great number of patients in a timely manner, in view of a potential clinical translation. Additionally, in this study we are interested in comparing numerical results in different patients rather than obtaining optimally accurate results for each patient. Since a fair comparison between patients is guaranteed by the adoption of the same assumptions, then we accept these simplifications.

Moreover, this study is subject to some further main limitations:

4) We focused on a single balloon-expandable TAVI valve type, the Edwards SAPIEN 23 mm (Section 2.1). Therefore, the results of our study, particularly the proposed SVD_{score}, cannot be generalized to different valves with different dimensions and designs, such as self-expandable valves. This is a consequence of the clinical data at disposal, related only to DEG patients who received an Edwards SAPIEN 23 *mm* valve. For coherence we considered also NODEG patients with an Edwards SAPIEN 23 *mm* to try to isolate the effect of hemodynamics on the development of SVD. Indeed, different valve designs can influence valve deterioration due, for example, to the different distribution of mechanical stresses [25] and the different material properties of the leaflets [72]. Future studies should focus on different valve designs to investigate if the biomechanical drivers of SVD identified here are still relevant.
5) We virtually inserted the bio-prosthetic valve in the aortic geometries assuming a perfect implantation, with the stent obtaining its nominal circular cross-section and being perfectly sealed to the aortic annulus (Section 2.2). On the other hand, the numerical simulation of the valve implantation using a structural Finite Element Analysis would allow to obtain the deformation of the stent shape due to a non-uniform bio-prosthetic valve expansion in a native calcified valve and to capture paravalvular leakage (PVL). This would influence the post-TAVI hemodynamic patterns in the aortic root and possibly would improve the quantitative agreement with the maximum blood velocity measurements, thus it should be considered in future studies. However, we justify this simplification since balloon-expandable valves are expected to achieve an almost cylindrical shape after implantation [73], as shown from the post-TAVI CTA scans reconstructions in [27], and since we are mainly interested in studying SVD rather than other complications related to the TAVI procedure.
6) We use PW Doppler TTE data, providing the temporal evolution of the blood velocity magnitude at the center of the LVOT, to derive a flow rate time-profile (Section 2.3) which we impose in our numerical simulations as an average condition using a Lagrange multiplier. In order to pass from a velocity measure, i.e. the velocity time-integral, to a flow measure, i.e. the cardiac output, in the clinical practice the velocity field in the LVOT is assumed to be uniform in space. In particular, to mitigate the effects of this a priori assumption, in this work we account for the same 15% overestimation of the flow rate in all the patients. Alternatively, one could derive a flow rate profile from the time-derivative of the left ventricular volume obtained from 3D echocardiography [74] or from Phase Contrast Cardiac Magnetic Resonance imaging techniques [75]. In this case, to obtain a flow rate measure, no a priori assumption on the spatial skewness of the velocity field is needed, thus potentially improving the accuracy of the resulting flow rate profile. Nonetheless, these data were not available for this retrospective study.
7) The significance of our findings is limited by the sample size of our study population. Therefore, enlarging the study population is crucial to move toward clinical relevance.

CRediT authorship contribution statement

Luca Crugnola: Writing – original draft, Visualization, Software, Project administration, Methodology, Investigation, Formal analysis, Data curation, Conceptualization. **Chiara Catalano:** Writing – review & editing, Methodology, Investigation, Formal analysis. **Laura Fusini:** Writing – review & editing, Supervision, Resources, Data curation, Conceptualization. **Salvatore Pasta:** Writing – review & editing, Supervision, Resources, Project administration. **Gianluca Pontone:** Writing – review & editing, Supervision, Resources, Project administration, Funding acquisition, Conceptualization. **Christian Vergara:** Writing – original draft, Validation, Supervision, Resources, Project administration, Methodology, Investigation, Funding acquisition, Data curation, Conceptualization.

Ethics approval

The study was approved by the Institutional Review Board of Centro Cardiologico Monzino on August 3rd, 2020 and registered with number R.1262/20-CCM 1326. Informed consent was obtained from all patients.

Funding

This research has been funded by the research program “Computational Prediction of TAVI Degeneration”. Funding: Monzino Cardiology Center, Milan.

Declaration of competing interest

The authors declare that they have no known competing financial interests or personal relationships that could have appeared to influence the work reported in this paper.

Acknowledgement

Luca Crugnola and Christian Vergara are members of the INdAM group GNCS “Gruppo Nazionale per il Calcolo Scientifico” (National Group for Scientific Computing).

We acknowledge the CINECA award under the ISCRA B and ISCRA C initiatives, for the availability of high-performance computing resources and support (ISCRA grants: IscrB_HPCHeart, P.I. Alfio Quarteroni; IscrC_TAVI-CFD, P.I. Luca Crugnola; IscrC_compTAVI, P.I. Luca Crugnola; IscrC_NM4CF, P.I. Francesca Renzi).

CV has been partially supported by: i) the European Union-Next Generation EU, Mission 4, Component 1, CUP: D53D23018770001, under the research project MIUR PRIN22-PNRR n.P20223KSS2, “Machine learning for fluid structure interaction in cardiovascular problems: efficient solutions, model reduction, inverse problems”, ii) the Italian Ministry of Health within the PNC PROGETTO HUB LIFE SCIENCE - DIAGNOSTICA AVANZATA (HLS-DA) “INNOVA”, PNCE3-2022–23683266–CUP: D43C22004930001, within the “Piano Nazionale Complementare Ecosistema Innovativo della Salute” - Codice univoco investimento: PNCE3-2022–23683266; iii) the Italian research project MIUR PRIN22 n.2022L3JC5T “Predicting the outcome of endovascular repair for thoracic aortic aneurysms: analysis of fluid dynamic modeling in different anatomical settings and clinical validation”; iv) Italian Ministry of Health within the project “CAL.HUB.RIA” - CALABRIA HUB PER RICERCA INNOVATIVA ED AVANZATA. Code: T4-AN-09, CUP: F63C22000530001.

Appendix A. On the definition of SVD

In this appendix we show that the definition of SVD adopted in this manuscript is in agreement with both the "stage 3 SVD" definition proposed by Dvir et al. in [30] and the definition of SVD with "Stage 3 Hemodynamic Valve Deterioration" proposed by the Valve Academic Research Consortium (VARC) 3 in [31].

We report in Table A.5 the PW and CW TTE data used to identify the onset of SVD at the long-term follow-up exam in all the patients in our study population. In particular, these data were acquired both early post-TAVI to obtain baseline measurements and at long-term follow-up to assess valve deterioration after some years. Additionally, we report in Table A.6 the absolute and relative difference between the long-term follow-up and the early post-TAVI data, for each type of data reported in Table A.5.

Dvir et al. defined "stage 3 SVD" as the development of severe stenosis and/or regurgitation in the implanted valve. In particular, severe stenosis is identified by the following characteristics [30]:

- Maximum blood velocity through the bio-prosthetic valve $V_{max} \geq 4.0\,[\frac{m}{s}]$;
- Mean transvalvular pressure gradient $\Delta P_{mean} \geq 40\,[mmHg]$;
- Absolute difference in mean gradient $D^{abs}_{\Delta P} \geq 20\,mmHg$;
- Doppler Velocity Index $DVI \leq 0.25$;
- Effective Orifice Area $EOA \leq 1.00$.

From Tables A.5 and A.6 we can see that, at the long-term follow-up exam, each DEG patients satisfies at least one of these conditions, whereas each NODEG does not satisfy any of these conditions.

On the other hand, the VARC 3 defines "Stage 3 Hemdoynamic Valve Deterioration" as an absolute difference in mean transvalvular pressure gradient $D^{abs}_{\Delta P} \geq 20\,mmHg$ resulting in a mean gradient $\Delta P^{F}_{mean} \geq 30\,[mmHg]$ with concomitant differences in Effective Orifice Area (EOA) $D^{abs}_{EOA} \leq -0.60\,cm^2$ or $D^{rel}_{EOA} \leq -50.0\,\%$ and/or differences in Doppler Velocity Index (DVI) $D^{abs}_{DVI} \leq -0.20$ or $D^{rel}_{DVI} \leq -40.0\,\%$. From Tables A.5 and A.6 we can see that, at the long-term follow-up exam, each DEG patients satisfies these conditions, whereas each NODEG does not satisfy these conditions.

Notice that the onset of SVD in patient DEG2 has been identified using the same criteria as for the other patients, but the early post-TAVI CW TTE data for this patients were not available at the time of this study. Thus, we could not report the differences between the long-term follow-up and the baseline measures.

Table A.5
Patients' data used to identify the onset of SVD. This data was obtain from early post-TAVI and long-term follow-up Pulsed Wave and Continuous Wave Transthoracic Echocardiography (TTE). The superscripts B and F identify the baseline and follow-up measurements, respectively. V^{*}_{max}: maximum velocity through the bio-prosthetic valve. ΔP^{*}_{mean}: mean transvalvular pressure gradient. EOA^{*}: Effective Orifice Area. DVI^{*}: Doppler Velocity Index.

ID	Early post-TAVI TTE				Long-term follow-up TTE			
	V^{B}_{max} $[\frac{m}{s}]$	ΔP^{B}_{mean} $[mmHg]$	EOA^{B} $[cm^2]$	DVI^{B} [-]	V^{F}_{max} $[\frac{m}{s}]$	ΔP^{F}_{mean} $[mmHg]$	EOA^{F} $[cm^2]$	DVI^{F} [-]
DEG1	2.6	15	1.67	0.48	4.0	40	1.02	0.36
DEG2	–	–	–	–	3.9	40	0.94	0.33
DEG4	2.6	13	1.64	0.43	4.0	40	0.81	0.26
DEG5	2.5	13	1.79	0.63	4.0	40	0.61	0.18
DEG6	2.6	14	1.87	0.45	4.0	35	1.18	0.34
DEG7	2.4	13	1.63	0.52	4.2	36	0.81	0.26
NODEG1	2.5	14	1.44	0.35	2.2	6	1.59	0.38
NODEG2	2.0	9	1.61	0.51	2.2	10	1.14	0.36
NODEG4	2.5	11	1.65	0.53	2.5	14	1.25	0.40
NODEG5	2.3	11	1.39	0.49	2.6	16	1.08	0.38
NODEG6	2.1	9	1.88	0.54	2.6	13	1.50	0.36
NODEG7	2.5	14	1.48	0.43	2.7	13	1.89	0.55

Table A.6
Differences between the long-term follow-up and early post-TAVI TTE data reported in Table A.5. The superscripts *abs* and *rel* identify the absolute and relative differences, respectively. D^{*}_{V} difference in terms of V_{max}. $D^{*}_{\Delta P}$ difference in terms of ΔP_{mean}. D_{EOA} difference in terms of EOA. D_{DVI} difference in terms of DVI.

ID	Absolute difference				Relative difference			
	D^{abs}_{V} $[\frac{m}{s}]$	$D^{abs}_{\Delta P}$ $[mmHg]$	D^{abs}_{EOA} $[cm^2]$	D^{abs}_{DVI} [-]	D^{rel}_{V} [%]	$D^{rel}_{\Delta P}$ [%]	D^{rel}_{EOA} [%]	D^{rel}_{DVI} [%]
DEG1	1.4	25	−0.65	−0.12	53.8	166.7	−38.9	−25.0
DEG2	–	–	–	–	–	–	–	–
DEG4	1.4	27	−0.83	−0.17	53.8	207.7	−50.6	39.5
DEG5	1.5	27	−1.18	−0.45	0.6	207.7	−65.9	−71.4
DEG6	1.4	21	−0.69	−0.11	53.8	150.0	−36.9	−24.4
DEG7	1.8	23	−0.82	−0.26	75.0	176.9	−50.3	−50.0
NODEG1	−0.3	−8	0.15	0.04	−12.0	−57.1	10.4	10.4
NODEG2	0.2	1	−0.47	−0.15	9.1	11.1	−29.2	−29.3
NODEG4	0.0	3	−0.40	−0.13	0.0	27.3	−24.2	−24.5
NODEG5	0.3	5	−0.31	−0.11	13.0	45.5	−22.3	−22.1
NODEG6	0.5	4	−0.38	−0.18	23.8	44.4	−20.2	−33.2
NODEG7	0.2	−1	0.41	0.12	8.0	−7.1	27.7	28.0

Appendix B. Mesh sensitivity analysis

B.1. Mesh size

In this section of the appendix we present the sensitivity analysis performed to choose the mesh size of our computational mesh (Fig. 3b). This is done to ensure that our numerical results do not strongly depend on the chosen mesh while allowing for a sustainable computational cost of the simulations. The analysis is carried out only for patient DEG1, as a representative of the study population, and we numerically simulate two complete heartbeats, analyzing only the results of the second one.

In our computational mesh the elements size is minimum at the level of the aortic annulus and a maximum at the level of the outlet section. We select the minimum element size on the aortic wall as a characteristic mesh size H and perform sequential refinements of the mesh by decreasing the value of H, while keeping the same ratio between the maximum and minimum element sizes. Specifically, we consider three refinement steps associated to $\{H_1, H_2, H_3\} = \{0.82, 0.65, 0.52\}$ mm, corresponding to computational meshes $\{M_1, M_2, M_3\}$, respectively. Let us define the refinement factor between two consecutive meshes as $R_i = \frac{H_{i+1}}{H_i}$, $i = 1, 2$. We deem a mesh as sufficiently refined if the relative difference between quantity of interest Q_{i+1}, computed in M_{i+1}, and Q_i, computed in M_i, is less than a tolerance $T(Q, R_i)$ which depends on the quantity of interest and the refinement factor. In particular, analogously to [76], we define the tolerance as follows:

$$T(Q, R_i) = \widehat{T}(Q)\cos\left(\frac{\pi}{2}R_i\right), \tag{B.1}$$

where $\widehat{T}(Q)$ represents an acceptable error with respect to the real measured quantity Q in the limit $R_i \to 0$, e.g. the uncertainty related to a clinical measure. This framework stresses the importance of taking into account the amount of refinement between meshes when quantifying the tolerance, with values of $R_i \approx 1$ resulting in $T(Q, R) \approx 0$.

We are interested in studying the WSS on the aortic wall, which highly depends on the mesh size. Thus, let us take as a quantity of interest the average-in-time maximum WSS value on the aortic wall $\overline{WSS^{max}}$ and set $\widehat{T}(\overline{WSS^{max}}) = 10\%$, since accurately computing the WSS is challenging even with the most sophisticated imaging techniques. We report

Table B.7
Mesh sensitivity analysis. i: refinement step; H_i: minimum element size on the aortic wall; R_i: refinement factor; $T(\overline{WSS^{max}}, R_i)$: tolerance; $E_i = \frac{|\overline{WSS^{max}}_{i+1} - \overline{WSS^{max}}_i|}{|\overline{WSS^{max}}_i^H|}$ relative difference. Mesh size.

i	Mesh	H_i	R_i	$T(\overline{WSS^{max}}, R_i)$	E_i
1	M_1	0.82 mm	0.79	3.24%	10.64%
2	M_2	0.65 mm	0.80	3.09%	1.16%
3	M_3	0.52 mm			

Table B.8
Sensitivity analysis on the number of sub-layers in the boundary layer. N_L: number of sub-layers; $\overline{WSS^{max}}$: the average-in-time of the maximum-in-space WSS magnitude on the aortic wall. E: relative difference.

NL	$\overline{WSS^{max}}\,[Pa]$	E
3	19.01	0.48%
5	18.92	

in Table B.7 the results of our analysis, showing that mesh M_2 is appropriately refined for our study. For the sake of completeness, in Fig. B.8 we plot the WSS on the aortic wall at the peak systolic flow instant for all the meshes, highlighting the similar results obtained for meshes M_2 ($H = 0.65$ mm) and M_3 ($H = 0.52$ mm).

B.2. Number of sub-layers in boundary layer

In this section of the appendix we present the sensitivity analysis performed to choose the number of sub-layers used to model the boundary layer in our computational mesh (Fig. 3b). This is done to ensure that our numerical results do not strongly depend on the chosen number of sub-layers while optimizing the computational cost of the simulations. The analysis is carried out only for patient DEG1, as a representative of the study population, and we numerically simulate two complete heartbeats, analyzing only the results of the second one.

In particular, we consider the number of sub-layers $N_L = \{3, 5\}$ and, analogously to the sensitivity analysis performed on the mesh size (Appendix B.1), we take as a quantity of interest the average-in-time maximum WSS value on the aortic wall $\overline{WSS^{max}}$. We report in Table B.8 the results of our analysis, showing that using $N_L = 3$ is enough to appropriately model the boundary layer.

For the sake of completeness, in Fig. B.9 we plot the WSS on the aortic wall at the peak systolic flow instant for both $N_L = 3$ and $N_L = 5$, highlighting the similar results obtained for these two choices.

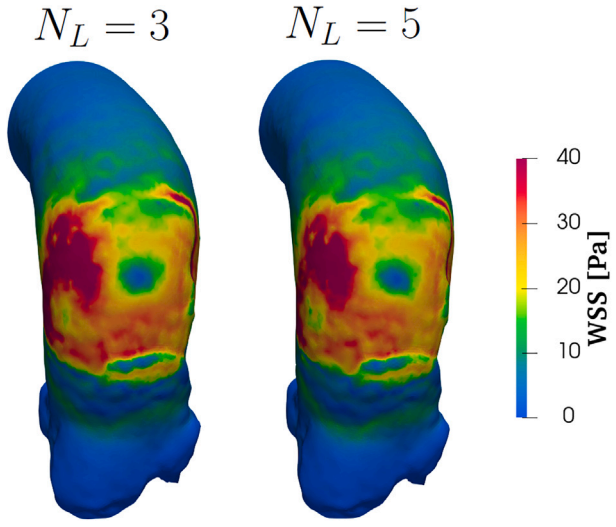

Fig. B.9. WSS on the aortic wall at the peak systolic flow instant with $N_L = 3$ (left), and with $N_L = 5$ (right).

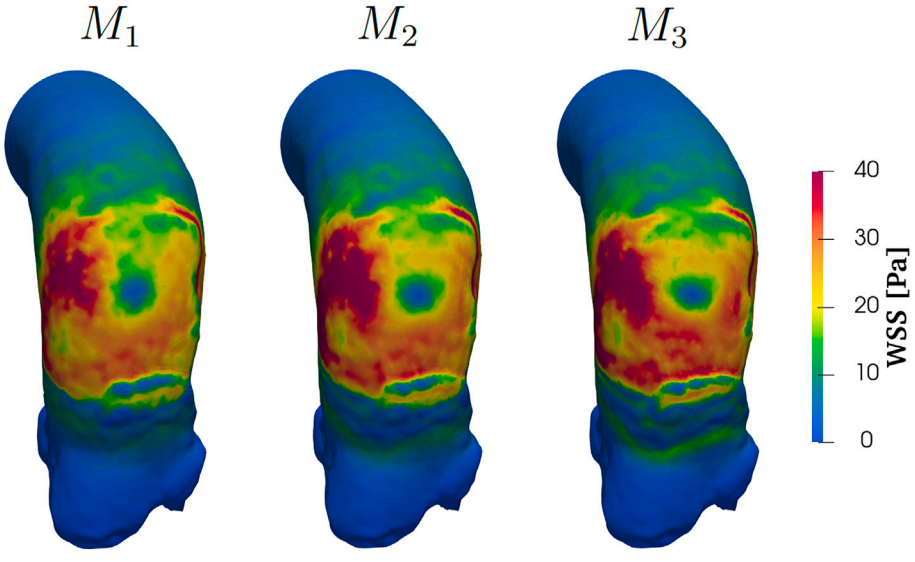

Fig. B.8. WSS on the aortic wall at the peak systolic flow instant in meshes M_1 ($H_1 = 0.82$ mm, left), M_2 ($H_2 = 0.65$ mm, center) and M_3 ($H_3 = 0.52$ mm, right).

References

[1] A. Vahanian, F. Beyersdorf, F. Praz, M. Milojevic, S. Baldus, J. Bauersachs, D. Capodanno, L. Conradi, M. De Bonis, R. De Paulis, V. Delgado, N. Freemantle, M. Gilard, K. H. Haugaa, A. Jeppsson, P. Jüni, L. Pierard, B. D. Prendergast, J. R. Sádaba, C. Tribouilloy, W. Wojakowski, E. S. D. Group, E. N. C. Societies, 2021 ESC/EACTS Guidelines for the management of valvular heart disease: Developed by the Task Force for the management of valvular heart disease of the European Society of Cardiology (ESC) and the European Association for Cardio-Thoracic Surgery (EACTS), Eur. Heart J. 43 (2021) 561–632.

[2] C.M. Otto, R.A. Nishimura, R.O. Bonow, B.A. Carabello, J.P. Erwin III, F. Gentile, H. Jneid, E.V. Krieger, M. Mack, C. McLeod, et al., 2020 ACC/AHA guideline for the management of patients with valvular heart disease: executive summary: a report of the american college of cardiology/american heart association joint committee on clinical practice guidelines, J. Am. Coll. Cardiol. 77 (2021) 450–500.

[3] M.J. Mack, M.B. Leon, V.H. Thourani, P. Pibarot, R.T. Hahn, P. Genereux, S.K. Kodali, S.R. Kapadia, D.J. Cohen, S.J. Pocock, et al., Transcatheter aortic-valve replacement in low-risk patients at five years, N. Engl. J. Med. 389 (2023) 1949–1960.

[4] J.K. Forrest, G.M. Deeb, S.J. Yakubov, H. Gada, M.A. Mumtaz, B. Ramlawi, T. Bajwa, P.S. Teirstein, D. Tchétché, J. Huang, et al., 4-year outcomes of patients with aortic stenosis in the evolut low risk trial, J. Am. Coll. Cardiol. 82 (2023) 2163–2165.

[5] J. Ternacle, S. Hecht, H. Eltchaninoff, E. Salaun, M.-A. Clavel, N. Côté, P. Pibarot, Durability of transcatheter aortic valve implantation, EuroIntervention 20 (2024) e845–e864.

[6] N. Côté, P. Pibarot, M.-A. Clavel, Incidence, risk factors, clinical impact, and management of bioprosthesis structural valve degeneration, Curr. Opin. Cardiol. 32 (2017) 123–129.

[7] A.E. Kostyunin, A.E. Yuzhalin, M.A. Rezvova, E.A. Ovcharenko, T.V. Glushkova, A.G. Kutikhin, Degeneration of bioprosthetic heart valves: update 2020, J. Am. Heart Assoc. 9 (2020) e018506.

[8] S.J. Bozso, J.J.H. Kang, R. Basu, B. Adam, J.R.B. Dyck, G.Y. Oudit, M.C. Moon, D.H. Freed, J. Nagendran, J. Nagendran, Structural valve deterioration is linked to increased immune infiltrate and chemokine expression, J. Cardiovasc. Transl. Res. 14 (2021) 503–512.

[9] S. Wen, Y. Zhou, W.Y. Yim, S. Wang, L. Xu, J. Shi, W. Qiao, N. Dong, Mechanisms and drug therapies of bioprosthetic heart valve calcification, Front. Pharmacol. 13 (2022) 909801.

[10] T. Rheude, C. Pellegrini, S. Cassese, J. Wiebe, S. Wagner, T. Trenkwalder, H. Alvarez, P. Mayr, C. Hengstenberg, H. Schunkert, A. Kastrati, O. Husser, M. Joner, Predictors of haemodynamic structural valve deterioration following transcatheter aortic valve implantation with latest-generation balloon-expandable valves, EuroIntervention 15 (2020) 1233–1239.

[11] M. Guglielmo, L. Fusini, M. Muratori, G. Tamborini, V. Mantegazza, D. Andreini, A. Annoni, M. Babbaro, A. Baggiano, E. Conte, et al., Computed tomography predictors of structural valve degeneration in patients undergoing transcatheter aortic valve implantation with balloon-expandable prostheses, Eur. Radiol. 32 (2022) 1–11.

[12] T.D. Tnay, D. Shell, A. Lui, Review of bioprosthetic structural valve deterioration: Patient or valve? J. Card. Surg. 37 (2022) 5243–5253.

[13] A. Ochi, K. Cheng, B. Zhao, A.A. Hardikar, K. Negishi, Patient risk factors for bioprosthetic aortic valve degeneration: a systematic review and meta-analysis, Heart Lung Circ. 29 (2020) 668–678.

[14] D. Carbonaro, D. Gallo, U. Morbiducci, A. Audenino, C. Chiastra, In silico biomechanical design of the metal frame of transcatheter aortic valves: multi-objective shape and cross-sectional size optimization, Struct. Multidiscip. Optim. 64 (2021) 1825–1842.

[15] B. Grossi, S. Barati, A. Ramella, F. Migliavacca, J.F.R. Matas, G. Dubini, N. Chakfé, F. Heim, O. Cozzi, G. Condorelli, et al., Validation evidence with experimental and clinical data to establish credibility of tavi patient-specific simulations, Comput. Biol. Med. 182 (2024) 109159.

[16] G. Luraghi, F. Migliavacca, A. García-González, C. Chiastra, A. Rossi, D. Cao, G. Stefanini, J.F.R. Matas, On the modeling of patient-specific transcatheter aortic valve replacement: a fluid–structure interaction approach, Cardiovasc. Eng. Technol. 10 (2019) 437–455.

[17] A.A. Basri, M. Zuber, E.I. Basri, M.S. Zakaria, A.F.A. Aziz, M. Tamagawa, K.A. Ahmad, Fluid structure interaction on paravalvular leakage of transcatheter aortic valve implantation related to aortic stenosis: A patient-specific case, Comput. Math. Methods Med. 2020 (2020) 9163085.

[18] M. Bianchi, G. Marom, R.P. Ghosh, O.M. Rotman, P. Parikh, L. Gruberg, D. Bluestein, Patient-specific simulation of transcatheter aortic valve replacement: impact of deployment options on paravalvular leakage, Biomech. Model. Mechanobiol. 18 (2019) 435–451.

[19] W. Mao, Q. Wang, S. Kodali, W. Sun, Numerical parametric study of paravalvular leak following a transcatheter aortic valve deployment into a patient-specific aortic root, J. Biomech. Eng. 140 (2018) 101007.

[20] G.M. Bosi, C. Capelli, M.H. Cheang, N. Delahunty, M. Mullen, A.M. Taylor, S. Schievano, A validated computational framework to predict outcomes in tavi, Sci. Rep. 10 (2020) 1–11.

[21] G. Rocatello, N. El Faquir, G. De Santis, F. Iannaccone, J. Bosmans, O. De Backer, L. Sondergaard, P. Segers, M. De Beule, P. de Jaegere, et al., Patient-specific computer simulation to elucidate the role of contact pressure in the development of new conduction abnormalities after catheter-based implantation of a self-expanding aortic valve, Circ. Cardiovasc. Interv. 11 (2018) e005344.

[22] M. Heitkemper, H. Hatoum, A. Azimian, B. Yeats, J. Dollery, B. Whitson, G. Rushing, J. Crestanello, S.M. Lilly, L.P. Dasi, Modeling risk of coronary obstruction during transcatheter aortic valve replacement, J. Thorac. Cardiovasc. Surg. 159 (2020) 829–838.

[23] C. Martin, W. Sun, Simulation of long-term fatigue damage in bioprosthetic heart valves: effects of leaflet and stent elastic properties, Biomech. Model. Mechanobiol. 13 (2014) 759–770.

[24] F. Sulejmani, A. Caballero, C. Martin, T. Pham, W. Sun, Evaluation of transcatheter heart valve biomaterials: computational modeling using bovine and porcine pericardium, J. Mech. Behav. Biomed. Mater. 97 (2019) 159–170.

[25] V. Stanová, R. Rieu, L. Thollon, E. Salaun, J. Rodés-Cabau, N. Côté, D. Mantovani, P. Pibarot, Leaflet mechanical stress in different designs and generations of transcatheter aortic valves: an in vitro study, Struct. Heart. 8 (2024) 100262.

[26] E. Tsolaki, P. Corso, R. Zboray, J. Avaro, C. Appel, M. Liebi, S. Bertazzo, P.P. Heinisch, T. Carrel, D. Obrist, et al., Multiscale multimodal characterization and simulation of structural alterations in failed bioprosthetic heart valves, Acta Biomater. 169 (2023) 138–154.

[27] L. Crugnola, C. Vergara, L. Fusini, I. Fumagalli, G. Luraghi, A. Redaelli, G. Pontone, Computational hemodynamic indices to identify transcatheter aortic valve implantation degeneration, Comput. Methods Programs Biomed. 259 (2025) 108517.

[28] I. Fumagalli, R. Polidori, F. Renzi, L. Fusini, A. Quarteroni, G. Pontone, C. Vergara, Fluid-structure interaction analysis of transcatheter aortic valve implantation, Int. J. Numer. Methods Biomed. Eng. 39 (2023) e3704.

[29] R.S. Rao, H. Maniar, A. Zajarias, Sapien valve: past, present, and future, Cardiac Interv Today 9 (2015) 35–41.

[30] D. Dvir, T. Bourguignon, C.M. Otto, R.T. Hahn, R. Rosenhek, J.G. Webb, H. Treede, M.E. Sarano, T. Feldman, H.C. Wijeysundera, et al., Standardized definition of structural valve degeneration for surgical and transcatheter bioprosthetic aortic valves, Circulation 137 (2018) 388–399.

[31] V.-.W. Committee, P. Généreux, N. Piazza, M.C. Alu, T. Nazif, R.T. Hahn, P. Pibarot, J.J. Bax, J.A. Leipsic, P. Blanke, et al., Valve academic research consortium 3: updated endpoint definitions for aortic valve clinical research, Eur. Heart J. 42 (2021) 1825–1857.

[32] L. Antiga, M. Piccinelli, L. Botti, B. Ene-Iordache, A. Remuzzi, D.A. Steinman, An image-based modeling framework for patient-specific computational hemodynamics, Med. Biol. Eng. Comput. 46 (2008) 1097–1112.

[33] T. Rheude, J. Blumenstein, H. Möllmann, O. Husser, Spotlight on the sapien 3 transcatheter heart valve, Med. Devices Evid. Res. (2018) 353–360.

[34] C. Catalano, T. Turgut, O. Zahalka, N. Götzen, S. Cannata, G. Gentile, V. Agnese, C. Gandolfo, S. Pasta, On the material constitutive behavior of the aortic root in patients with transcatheter aortic valve implantation, Cardiovasc. Eng. Technol. 15 (2024) 95–109.

[35] N. Holoshitz, C.J. Kavinsky, Z.M. Hijazi, The edwards sapien transcatheter heart valve for calcific aortic stenosis: a review of the valve, procedure, and current literature, Cardiol. Ther. 1 (2012) 6.

[36] K. Capellini, E. Vignali, E. Costa, E. Gasparotti, M.E. Biancolini, L. Landini, V. Positano, S. Celi, Computational fluid dynamic study for ataa hemodynamics: an integrated image-based and radial basis functions mesh morphing approach, J. Biomech. Eng. 140 (2018).

[37] O. Rossvoll, S. Samstad, H.G. Torp, D.T. Linker, T. Skjærpe, B.A.J. Angelsen, L. Hatle, The velocity distribution in the aortic anulus in normal subjects: a quantitative analysis of two-dimensional doppler flow maps, J. Am. Soc. Echocardiogr. 4 (1991) 367–378.

[38] H. Liu, L. Lan, J. Abrigo, H.L. Ip, Y. Soo, D. Zheng, K.S. Wong, D. Wang, L. Shi, T.W. Leung, et al., Comparison of newtonian and non-newtonian fluid models in blood flow simulation in patients with intracranial arterial stenosis, Front. Physiol. 12 (2021) 718540.

[39] A.D. Caballero, S.J.C.E. Laín, A review on computational fluid dynamics modelling in human thoracic aorta, Cardiovasc. Eng. Technol. 4 (2013) 103–130.

[40] A. Leuprecht, S. Kozerke, P. Boesiger, K. Perktold, Blood flow in the human ascending aorta: a combined mri and cfd study, J. Eng. Math. 47 (2003) 387–404.

[41] P.D. Stein, H.N. Sabbah, Turbulent blood flow in the ascending aorta of humans with normal and diseased aortic valves, Circ. Res. 39 (1976) 58–65.

[42] E.L. Manchester, S. Pirola, M.Y. Salmasi, D.P. O'Regan, T. Athanasiou, X.Y. Xu, Analysis of turbulence effects in a patient-specific aorta with aortic valve stenosis, Cardiovasc. Eng. Technol. 12 (2021) 438–453.

[43] F. Nicoud, H.B. Toda, O. Cabrit, S. Bose, J. Lee, Using singular values to build a subgrid-scale model for large eddy simulations, Phys. Fluids 23 (2011) 085106.

[44] M. Rieth, F. Proch, O.T. Stein, M.W.A. Pettit, A.M. Kempf, Comparison of the sigma and smagorinsky les models for grid generated turbulence and a channel flow, Comput. Fluids 99 (2014) 172–181.

[45] M. Fedele, E. Faggiano, L. Dedè, A. Quarteroni, A patient-specific aortic valve model based on moving resistive immersed implicit surfaces, Biomech. Model. Mechanobiol. 16 (2017) 1779–1803.

[46] A. Veneziani, C. Vergara, Flow rate defective boundary conditions in haemodynamics simulations, Int. J. Numer. Methods Fluids 47 (2005) 803–816.

[47] L. Formaggia, J.-F. Gerbeau, F. Nobile, A. Quarteroni, Numerical treatment of defective boundary conditions for the navier–stokes equations, SIAM J. Numer. Anal. 40 (2002) 376–401.

[48] L. Bennati, Image-based numerical modeling of blood dynamics in presence of regurgitant and repaired mitral valve, (Ph.D. thesis), Università Degli Studi Di Verona, 2024.

[49] L. Bennati, A. Crispino, C. Vergara, Computational modeling of cardiac hemodynamics including chordae tendineae, papillaries, and valves dynamics, Comput. Biol. Med. 186 (2025) 109658.

[50] T.E. Tezduyar, Stabilized finite element formulations for incompressible flow computations, Adv. Appl. Mech. 28 (1991) 1–44.
[51] M.E. Moghadam, Y. Bazilevs, T.-Y. Hsia, I.E. Vignon-Clementel, A.L. Marsden, A comparison of outlet boundary treatments for prevention of backflow divergence with relevance to blood flow simulations, Comput. Mech. 48 (2011) 277–291.
[52] Y. Saad, Iterative methods for sparse linear systems, SIAM, 2003.
[53] L. Crugnola, C. Vergara, Inexact block lu preconditioners for incompressible fluids with flow rate conditions, CiCP 39 (2026) 323–355.
[54] P.C. Africa, lifex: A flexible, high performance library for the numerical solution of complex finite element problems, SoftwareX 20 (2022) 101252.
[55] P.C. Africa, I. Fumagalli, M. Bucelli, A. Zingaro, M. Fedele, A. Quarteroni, et al., lifex-cfd: An open-source computational fluid dynamics solver for cardiovascular applications, Comput. Phys. Commun. 296 (2024) 109039.
[56] U. Morbiducci, V. Mazzi, M. Domanin, G. De Nisco, C. Vergara, D.A. Steinman, D. Gallo, Wall shear stress topological skeleton independently predicts long-term restenosis after carotid bifurcation endarterectomy, Ann. Biomed. Eng. 48 (2020) 2936–2949.
[57] L. Chen, H. Deng, H. Cui, J. Fang, Z. Zuo, J. Deng, Y. Li, X. Wang, L. Zhao, Inflammatory responses and inflammation-associated diseases in organs, Oncotarget 9 (2017) 7204.
[58] P. Eshtehardi, A.J. Brown, A. Bhargava, C. Costopoulos, O. Hung y, M.T. Corban, H. Hosseini, B.D. Gogas, D.P. Giddens, H. Samady, High wall shear stress and high-risk plaque: an emerging concept, Int. J. Cardiovasc. Imaging 33 (2017) 1089–1099.
[59] A. Arzani, S.C. Shadden, Wall shear stress fixed points in cardiovascular fluid mechanics, J. Biomech. 73 (2018) 145–152.
[60] L. Chen, H. Qu, B. Liu, B.-C. Chen, Z. Yang, D.-Z. Shi, Y. Zhang, Low or oscillatory shear stress and endothelial permeability in atherosclerosis, Front. Physiol. 15 (2024) 1432719.
[61] L.J. Frazin, D.D. McPherson, D.J. Mehlman, K.B. Chandran, Functional chiral asymmetry in the descending thoracic aorta, Circulation 83 (1991) 712.
[62] P.J. Kilner, G.Z. Yang, R.H. Mohiaddin, D.N. Firmin, D.B. Longmore, Helical and retrograde secondary flow patterns in the aortic arch studied by three-directional magnetic resonance velocity mapping, Circulation 88 (1993) 2235–2247.
[63] P. Di Achille, G. Tellides, C.A. Figueroa, J.D. Humphrey, A haemodynamic predictor of intraluminal thrombus formation in abdominal aortic aneurysms, Proc. R. Soc. A: Math. Phys. Eng. Sci. 470 (2014) 20140163.
[64] H. Wang, D. Balzani, V. Vedula, K. Uhlmann, F. Varnik, On the potential self-amplification of aneurysms due to tissue degradation and blood flow revealed from fsi simulations, Front. Physiol. 12 (2021) 785780.
[65] C. Trenti, M. Ziegler, N. BjarnegÃ, T. Ebbers, M. Lindenberger, P. Dyverfeldt, et al., Wall shear stress and relative residence time as potential risk factors for abdominal aortic aneurysms in males: a 4D flow cardiovascular magnetic resonance caseâ€“control study, J. Cardiovasc. Magn. Reson. 24 (2022) 18.
[66] E.Y.L. Lui, A.H. Steinman, R.S.C. Cobbold, K.W. Johnston, Human factors as a source of error in peak doppler velocity measurement, J. Vasc. Surg. 42 (2005) 972–e1.
[67] J. Niederberger, H. Schima, G. Maurer, H. Baumgartner, Importance of pressure recovery for the assessment of aortic stenosis by doppler ultrasound: role of aortic size, aortic valve area, and direction of the stenotic jet in vitro, Circulation 94 (1996) 1934–1940.
[68] R.F. Siddiqui, J.R. Abraham, J. Butany, Bioprosthetic heart valves: modes of failure, Histopathology 55 (2009) 135–144.
[69] S. Madhavan, E.M.C. Kemmerling, The effect of inlet and outlet boundary conditions in image-based cfd modeling of aortic flow, Biomed. Eng. Online 17 (2018) 66.
[70] A. Quarteroni, A. Manzoni, C. Vergara, The cardiovascular system: mathematical modelling, numerical algorithms and clinical applications, Acta Numerica 26 (2017) 365–590.
[71] F.L. Abel, Influence of aortic compliance on coronary blood flow, Circ. Shock 12 (1984) 265–276.
[72] Y. Kang, H.Y. Hwang, S.H. Sohn, J.W. Choi, K.H. Kim, K.-B. Kim, Comparative analysis of structural valve deterioration after bioprosthetic tricuspid valve replacement: bovine pericardial versus porcine valves, Artif. Organs. 45 (2021) 911–918.
[73] J. Li, W. Yan, W. Wang, S. Wang, L. Wei, Comparison of balloon-expandable valve and self-expandable valve in transcatheter aortic valve replacement: A patient-specific numerical study, J. Biomech. Eng. 144 (2022) 104501.
[74] P.-M. Jokiel, T. Schweizer, D.P. Guensch, D. Berdajs, J. Erb, D. Bolliger, F. Kamber, E. Mauermann, Estimation of systolic and diastolic left ventricular blood flow from derivatives of transesophageal echocardiographic 3D volume curves in cardiac surgery patients: a proof-of-concept study, Semin. Cardiothorac. Vasc. Anesth. 28 (2024) 195–202.
[75] A. Sun, B. Zhao, Y. Li, Q. He, R. Li, C. Yuan, Real-time phase-contrast flow cardiovascular magnetic resonance with low-rank modeling and parallel imaging, J. Cardiovasc. Magn. Reson. 19 (2016) 19.
[76] F. Duca, D. Bissacco, L. Crugnola, C. Faitini, M. Domanin, F. Migliavacca, S. Trimarchi, C. Vergara, Computational analysis to assess hemodynamic forces in descending thoracic aortic aneurysms, J. Physiol. (2025).